The Astrophysical Journal, 983:86 (13pp), 2025 April 10 https://doi.org/10.3847/1538-4357/adb428

Discovery and Extensive Follow-up of SN 2024ggi, a Nearby Type IIP Supernova in NGC 3621

Ting-Wan Chen (陳婷琬)[1], Sheng Yang (杨圣)[2], Shubham Srivastav[3], Takashi J. Moriya[4,5,6], Stephen J. Smartt[3,7], Sofia Rest[8], Armin Rest[9,10], Hsing Wen Lin (林省文)[11], Hao-Yu Miao (繆皓宇)[1], Yu-Chi Cheng (鄭宇棋)[12,13], Amar Aryan[1], Chia-Yu Cheng (鄭家羽)[1], Morgan Fraser[14], Li-Ching Huang (黃立晴)[12,13], Meng-Han Lee (李孟翰)[1], Cheng-Han Lai (賴政翰)[1], Yu-Hsuan Liu (劉宇軒)[1,15], Aiswarya Sankar.K[1], Ken W. Smith[7], Heloise F. Stevance[3,7], Ze-Ning Wang (王泽宁)[2,16], Joseph P. Anderson[17,18], Charlotte R. Angus[7], Thomas de Boer[19], Kenneth Chambers[19], Hao-Yuan Duan (段皓元)[20], Nicolas Erasmus[21], Michael Fulton[7], Hua Gao[19], Joanna Herman[19], Wei-Jie Hou (侯偉傑)[1], Hsiang-Yao Hsiao (蕭翔耀)[1], Mark E. Huber[19], Chien-Cheng Lin (林建爭)[19], Hung-Chin Lin (林宏欽)[1], Eugene A. Magnier[19], Ka Kit Man (文家傑)[22], Thomas Moore[7,17], Chow-Choong Ngeow (饒兆聰)[1], Matt Nicholl[7], Po-Sheng Ou (歐柏昇)[23,15], Giuliano Pignata[24,18], Yu-Chien Shiau (蕭聿謙)[25], Julian Silvester Sommer[26], John L. Tonry[19], Xiao-Feng Wang (王晓锋)[27,28], Richard Wainscoat[19], David R. Young[7], You-Ting Yeh (葉祐廷)[29], and Jujia Zhang (张居甲)[30,31]

[1] Graduate Institute of Astronomy, National Central University, 300 Jhongda Road, 32001 Jhongli, Taiwan; twchen@astro.ncu.edu.tw
[2] Henan Academy of Sciences, Zhengzhou 450046, Henan, People's Republic of China; sheng.yang@hnas.ac.cn
[3] Astrophysics Sub-Department, Department of Physics, University of Oxford, Keble Road, Oxford, OX1 3RH, UK
[4] National Astronomical Observatory of Japan, National Institutes of Natural Sciences, 2-21-1 Osawa, Mitaka, Tokyo 181-8588, Japan
[5] Graduate Institute for Advanced Studies, SOKENDAI, 2-21-1 Osawa, Mitaka, Tokyo 181-8588, Japan
[6] School of Physics and Astronomy, Monash University, Clayton, VIC 3800, Australia
[7] Astrophysics Research Centre, School of Mathematics and Physics, Queen's University Belfast, BT7 1NN, UK
[8] Department of Computer Science, The Johns Hopkins University, Baltimore, MD 21218, USA
[9] Space Telescope Science Institute, 3700 San Martin Drive, Baltimore, MD 21218, USA
[10] Department of Physics and Astronomy, Johns Hopkins University, Baltimore, MD 21218, USA
[11] Department of Physics, University of Michigan, 450 Church Street, Ann Arbor, MI 48109-1107, USA
[12] Department of Physics, National Taiwan Normal University, No. 88, Sect. 4, Tingzhou Road, Wenshan Dist., Taipei City, 116325, Taiwan
[13] Center of Astronomy and Gravitation, National Taiwan Normal University, No. 88, Sect. 4, Tingzhou Road, Wenshan Dist., Taipei City, 116325, Taiwan
[14] School of Physics, O'Brien Centre for Science North, University College Dublin, Belfield, Dublin 4, Ireland
[15] Institute of Astronomy and Astrophysics, Academia Sinica, No. 1, Sec. 4, Roosevelt Road, Taipei 106216, Taiwan
[16] School of Physics, Henan Normal University, Xinxiang 453007, Henan, People's Republic of China
[17] European Southern Observatory, Alonso de Córdova 3107, Casilla 19, Santiago, Chile
[18] Millennium Institute of Astrophysics MAS, Nuncio Monseñor Sotero Sanz 100, Off. 104, Providencia, Santiago, Chile
[19] Institute for Astronomy, University of Hawai'i, 2680 Woodlawn Drive, Honolulu, HI 96822, USA
[20] Taipei Astronomical Museum, Taipei, Taiwan
[21] South African Astronomical Observatory, 1 Observatory Road, Cape Town, 7925, South Africa
[22] School of Business, Hong Kong Baptist University, Hong Kong
[23] Department of Physics, National Taiwan University, No. 1, Sec. 4, Roosevelt Road, Taipei 106216, Taiwan
[24] Instituto de Alta Investigación, Universidad de Tarapacá, Casilla 7D, Arica, Chile
[25] Taipei Amateur Astronomers Association
[26] Universitäts-Sternwarte, Fakultät für Physik, Ludwig-Maximilians Universität, Scheinerstr. 1, 81679 München, Germany
[27] Physics Department, Tsinghua University, Beijing, 100084, People's Republic of China
[28] Purple Mountain Observatory, Chinese Academy of Science, Nanjing, 210023, People's Republic of China
[29] CheCheng Elementary School Observatory, Taiwan
[30] Yunnan Observatories (YNAO), Chinese Academy of Sciences (CAS), Kunming, 650216, People's Republic of China
[31] International Centre of Supernovae, Yunnan Key Laboratory, Kunming 650216, People's Republic of China
Received 2024 June 17; revised 2025 January 4; accepted 2025 January 11; published 2025 April 9

Abstract

We present the discovery and early observations of the nearby Type II supernova (SN) 2024ggi in NGC 3621 at 6.64 ± 0.3 Mpc. The SN was caught $5.8^{+1.9}_{-2.9}$ hr after its explosion by the ATLAS survey. Early-phase, high-cadence, and multiband photometric follow-up was performed by the Kilonova Finder (Kinder) project, collecting over 1000 photometric data points within 1 week. The combined *o*- and *r*-band light curves show a rapid rise of 3.3 mag in 13.7 hr, much faster than SN 2023ixf (another nearby and well-observed SN II). Between 13.8 and 18.8 hr after explosion, SN 2024ggi became bluer, with $u - g$ color dropping from 0.53 to 0.15 mag. The rapid blueward evolution indicates a wind shock breakout (SBO) scenario. No hour-long brightening expected for the SBO from a bare stellar surface was detected during our observations. The classification spectrum, taken 17 hr after the SN explosion, shows flash features of high-ionization species such as Balmer lines, He I, C III, and N III. Detailed light-curve modeling provides critical insights into the circumstellar material (CSM). Our favored model has an explosion energy of 2×10^{51} erg, a mass-loss rate of $10^{-3}\,M_{\odot}\,\mathrm{yr}^{-1}$ (with an assumed 10 km s^{-1} wind), and

a confined CSM radius of 6×10^{14} cm. The corresponding CSM mass is $0.4\,M_{\odot}$. Comparisons with SN 2023ixf highlight that SN 2024ggi has a less dense confined CSM, resulting in a faster rise and fainter UV flux. Citizen astronomer collaboration and extensive data are essential for SBO searches and detailed SN characterizations.

Unified Astronomy Thesaurus concepts: Type II supernovae (1731); Supernovae (1668); Core-collapse supernovae (304)

Materials only available in the online version of record: machine-readable table

1. Introduction

Core-collapse supernovae (SNe) mark the end stage of massive ($>8\,M_{\odot}$) star evolution. Those that have hydrogen present in their spectra are classified as Type II SNe. Within this category, some display a plateau in their light curves (Type IIP), which is thought to result from the hydrogen recombination in the expanding ejecta. Capturing such events as early as possible is crucial for detecting the phenomenon known as shock breakout (SBO), where the SN shock wave emerges from the stellar surface or from dense circumstellar material (CSM) surrounding the progenitor. If the CSM is not dense, this SBO event can be marked by a brief but intense burst of high-energy radiation, providing direct insights into the outermost layers of the progenitor star (e.g., E. Waxman & B. Katz 2017). If the CSM is dense and optically thick enough, SBO occurs within the CSM. In such a case, we do not expect to observe the brief but intense burst because of photon diffusion in the dense CSM, but the early optical light curves evolve more quickly (e.g., T. Moriya et al. 2011; T. J. Moriya et al. 2018; V. Morozova et al. 2017, 2018). Such a quick rise is often observed in SNe II (e.g., S. González-Gaitán et al. 2015; F. Förster et al. 2018). J. A. Goldberg et al. (2022) suggest that the absence of a detected SBO signature can be attributed to the realistic 3D structure of a red supergiant (RSG), which includes large convective bubbles at the photosphere (as observed in Betelgeuse). This structure spreads the SBO over a longer duration, resulting in a fainter signal.

If caught early, SN II spectra can show narrow emission lines of high-ionization species (e.g., V. S. Niemela et al. 1985; A. Gal-Yam et al. 2014). These "flash" features disappear within hours to days and result from the interaction of the SN shock wave with CSM surrounding the progenitor star. These flash spectra provide a detailed view of the immediate environment of the progenitor star and the recent mass-loss history in the narrow window between core collapse and the ejecta sweeping up the immediate surroundings. Sample studies suggest that more than 40% of SNe II discovered within 2 days of first light show flash features from interaction with dense CSM (R. J. Bruch et al. 2021, 2023). SN 2023ixf is a notable recent example of a flash SN IIP, discovered early by a citizen astronomer (K. Itagaki 2023) and monitored extensively (e.g., K. A. Bostroem et al. 2023; J. Zhang et al.2023).

SN 2024ggi is one of the nearest SNe of the present decade (S. Srivastav et al. 2024; J. Tonry et al. 2024; for full details, see Section 2), following SN 2014J in M82 (Type Ia; S. J. Fossey et al. 2014) and SN 2023ixf in M101. Its host galaxy, NGC 3621, is a well-known spiral galaxy located only 6.64 Mpc away (for more details, see Appendix D). SN 2024ggi was discovered very early (for more details, see Section 3.2) by the Asteroid Terrestrial-impact Last Alert System (ATLAS) and has been exceptionally well monitored with multiwavelength observations: γ-ray (G. Marti-Devesa & Fermi-LAT Collaboration 2024), X-ray (J. Zhang et al. 2024a), optical (T. W. Chen et al. 2024; T. Killestein et al. 2024; B. Kumar et al. 2024; F. D. Romanov 2024), radio (S. Ryder et al. 2024), and limits at centimeter wavelengths (P. Chandra et al. 2024). W. Hoogendam et al. (2024) and Q. Zhai et al. (2024a) obtained spectra for SN 2024ggi, classifying it as a young Type II SN with flash ionization features (we present one classification spectrum in Section 2.6). Further well-analyzed data sets of early spectroscopy within 1–2 days after the SN discovery have been presented in W. V. Jacobson-Galán et al. (2024), T. Pessi et al. (2024), M. Shrestha et al. (2024), and J. Zhang et al. (2024b). These spectra displayed strong and narrow features of high-ionization species including He I, He II, N III, C III, N IV, and C IV. Later on, a rise in ionization was also observed as indicated by the presence of He II, C IV, N IV/V, and O V features. Several groups searched for the progenitor star using the archival imaging from the Hubble Space Telescope (HST), Dark Energy Camera Legacy Survey, and XMM-Newton (X. Chen et al. 2024; Y. Komura et al. 2024; I. Pérez-Fournon et al. 2024; S. Srivastav et al. 2024; S. Yang et al. 2024). Utilizing the preexplosion images from HST and the Spitzer Space Telescope, D. Xiang et al. (2024) found that SN 2024ggi probably resulted from the explosion of a solar-metallicity massive star having an initial mass of $13^{+1}_{-1}\,M_{\odot}$.

In this paper, we report the discovery of SN 2024ggi, and we focus on its early photometric and spectroscopic observations in Section 2, including images contributed by citizen scientists. In Section 3, we highlight the importance of early detection and high-cadence monitoring for uncovering the details of SN 2024ggi, such as searching precursors and SBO signals, constructing a bolometric light curve, temperature, and radius evolution. In Section 4, we model the light curve to estimate CSM properties, discuss our results, and compare the properties of SN 2024ggi to several classical Type II SNe, particularly SN 2023ixf. Finally, we conclude our findings in Section 5. Throughout this paper, all magnitudes are reported in the AB system.

2. Observations

2.1. ATLAS Discovery of SN 2024ggi

ATLAS (J. L. Tonry et al. 2018a) comprises a network of four 0.5 m telescopes located in Hawaii, Chile, and South Africa, facilitating wide-field all-sky observations. These telescopes continuously scan the entire visible sky, completing approximately four scans within a 24 hr period when all units are operational. Following data acquisition, automated image processing occurs (J. L. Tonry et al. 2018a) incorporating photometric and astrometric calibration procedures using the reference catalog RefCat2 (J. L. Tonry et al. 2018b). Subsequently, a reference image is subtracted to find transient events. The significant sources detected on the difference images are filtered through a transient discovery pipeline (the ATLAS Transient Server; K. W. Smith et al. 2020). This

streamlined process enables rapid identification of extragalactic transients, and all data can be accessed[32] through our forced photometry server (L. Shingles et al. 2021).

Our ATLAS Transient Server requires three or more spatially coincident detections (with a significance of at least 5σ) of a source to trigger it as an object for further processing (see K. W. Smith et al. 2020 for more details). The three detections of the source internally labeled as ATLAS24fsk and automatically associated with the nearby galaxy NGC 3621 were made on 2024 April 11 at UT 03:23 (MJD = 60411.141), UT 05:36 (60411.234), and UT 06:01 (60411.251) in 110 s exposures. The three detections indicated a rapidly brightening transient on the *orange* (o) filter, analogous to the Pan-STARRS Sloan Digital Sky Survey (SDSS) $r + i$ filters. With the first detection at $o = 18.95 \pm 0.10$, the three detections immediately revealed a rapid intranight rise of 1.03 mag over a span of 2.64 hr. This implies an absolute magnitude of $M_o = -10.32$ to -11.35 mag after Milky Way extinction correction ($A_o = (A_r + A_i)/2 = 0.16$; E. F. Schlafly & D. P. Finkbeiner 2011) and adopting a host distance modulus of $\mu = 29.11$ at a luminosity distance of 6.64 Mpc (for further discussion of distance, see Appendix D). We immediately posted the discovery on the Transient Name Server,[33] with the IAU name AT 2024ggi at sky coordinates of R.A. = 169.59207 and decl. = −32.83759 ($11^h18^m22\overset{s}{.}09$, $-32°50'15\overset{''}{.}3$; J. Tonry et al. 2024) on 2024 April 11 09:03 UT. We also posted an AstroNote to draw attention to the discovery (S. Srivastav et al. 2024). We had a gap in observations prior to this mostly due to weather, with the last nondetection 6 days prior on MJD 60405.063, with an o-band limit of 19.8 mag. This is not a constraining limit, but the rapid rise within the 2.64 hr spanning the exposures indicated that this was likely a very young SN. Figure 1 shows the discovery image, along with the reference and the subtracted frames. We conducted a search for precursors in the history of forced photometry in ATLAS (see Section 3.1 for details).

2.2. Kinder Early-phase, High-cadence Follow-up

The Kilonova Finder (Kinder) project is dedicated to rapidly identify fast-evolving transients, especially those displaying blue/red colors and rapid fading characteristics, with the specific aim of detecting kilonovae. We use the 40 cm SLT telescope at Lulin Observatory in Taiwan as the primary instrument for observing newly discovered nearby transients within 100 Mpc found by ATLAS, hence exploiting the longitude difference as night hours move west. Equipped with standard SDSS filters (u', g', r', i', and z'), the SLT facilitates the efficient selection of objects exhibiting significant color indices. Moreover, we have developed a dedicated pipeline, known as Kinder-pip (S. Yang et al. 2021), to perform image subtractions using archival images sourced from databases such as the SDSS, Pan-STARRS1 (PS1), and DESI legacy survey. Since its first follow-up campaign in 2021 (T. W. Chen et al. 2021), the Kinder project has investigated over 280 objects, with some being used in detailed single-object studies (J. H. Gillanders et al. 2024; T. Moore et al. 2025; J. Pearson et al. 2024).

During the ATLAS eyeballing process of the initial three detections of SN 2024ggi, we triggered multiband follow-up imaging observations with SLT in order to confirm this discovery and further constrain the rapidly evolving light curve. Thanks to Lulin Observatory's longitude, we were well placed to rapidly slew to SN 2024ggi following the ATLAS discovery. Observations started at 11:24 UT on 2024 April 11 (MJD = 60411.476) as soon as the target was visible during evening twilight. We clearly detected SN 2024ggi in the first u- and g-band raw images and confirmed it as a real source, prompting the ATLAS team to publish the AstroNote (S. Srivastav et al. 2024) describing the discovery. Following image reduction and photometric measurements, we identified SN 2024ggi to be a blue and fast-evolving transient: in particular, the r band exhibited a sharp rise of 2.56 mag in 8.26 hr compared to the ATLAS o-band discovery. Our results were reported to Transient Name Server (TNS) in T. W. Chen et al. (2024). Concurrently, the GOTO project also reported a similar magnitude (T. Killestein et al. 2024). We conducted continuous observations of SN 2024ggi using SLT. On the first night, the observing conditions were good (with seeing around $1\overset{''}{.}2$), and observations were carried out down to a very high air mass (4.42), which allowed 6 hr of continuous coverage of the early rise of the light curve. We obtained a total of 53 frames. The brightness increased by 1.2 mag in the u band and by 0.8, 0.7, 0.5, and 0.6 in the g, r, i, and z bands, respectively.

We employed Kinder-pip (S. Yang et al. 2021) to conduct aperture photometry for SN 2024ggi without template subtraction. Magnitudes were determined by calibrating against SkyMapper field stars. We report the first epoch of each band's magnitude in Table 1 and the complete measurements in a dedicated machine-readable table. In addition, we measured the magnitudes using various methods, including aperture and point-spread function (PSF) photometry, both with and without template subtraction (against the archival Legacy Survey template images). The results are generally consistent, despite a few early points showing a 0.2 mag difference. Due to the lack of u-band template images, we decided to present and adopt the aperture photometry without template subtraction in this paper to maintain uniformity. However, for specific cases like searching for SBO emissions in the early phases, we used PSF magnitudes after template subtraction instead. Measurements obtained through different methods will be made publicly available in a machine-readable table as well. The bottom left panel of Figure 1 displays a color-composite image from SLT images.

2.3. Citizen Science Images

Citizen science images regularly contribute valuable data for discovering and studying SNe, especially during the early phases, which are crucial for constraining the explosion time and rise, and investigating SBO phenomena (e.g., SN 2023ixf, G. Hosseinzadeh et al. 2023; K. Itagaki 2023; O. Yaron et al. 2023; G. Li et al. 2024). Based on our experience with SN 2023ixf (T. Chen et al. 2023), we requested early-phase images of SN 2024ggi via the Astronomical Association of Taichung Facebook group page. Five groups, including citizen astronomers Shiau, Man, and Kuo, as well as the CheCheng Elementary School Observatory (CCESO) and Taipei Astronomical Museum (TAM), provided data taken from 2024 April 11.52 to 2024 April 20.58 (Table 1). Unlike M101, NGC 3621 is less popular among citizen scientists and has low-altitude visibility from Taiwan, resulting in no prediscovery observations.

[32] https://fallingstar.com
[33] https://www.wis-tns.org/object/2024ggi

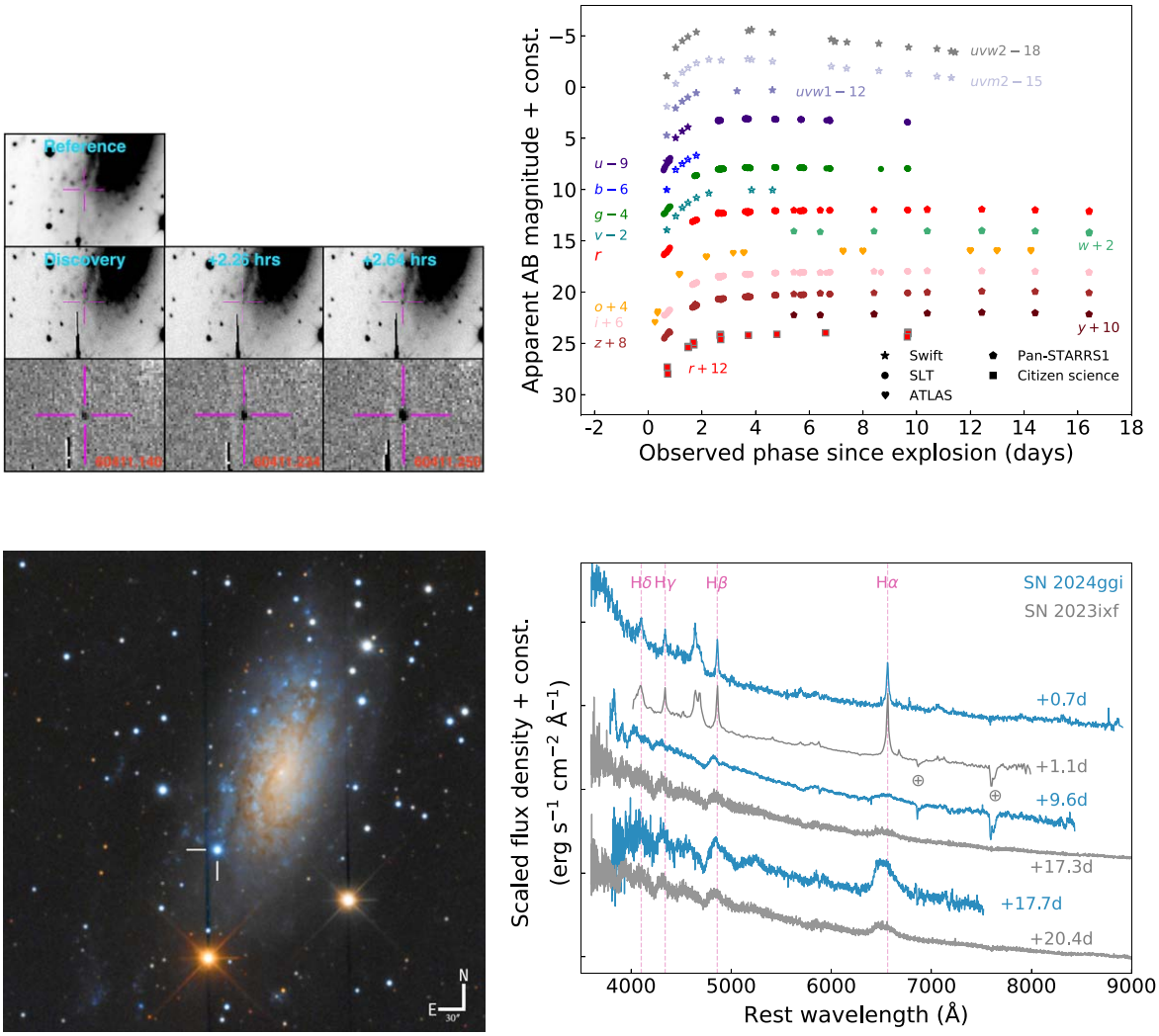

Figure 1. Upper left panel: ATLAS prediscovery, discovery, and rapid follow-up images of SN 2024ggi are presented, with their corresponding subtracted images (observed MJD shown in red) displayed at the bottom. Bottom left panel: a *gri* color-composite image of SN 2024ggi, its host galaxy, and the environment. This image was created using SLT *g*-, *r*-, and *i*-band (blue, green, and red, respectively) images taken between 2024 April 11 and 2024 April 20. We homogenized the background flux, combined the images using median stacking, and processed them with `PixInsight` to enhance color and contrast. Upper right panel: multiband light curves of SN 2024ggi. The citizen science images are provided by Shiau and Man, as well as the TAM and CCESO. We converted these magnitudes to the *r* band. Bottom right panel: spectroscopic evolution of SN 2024ggi and comparison with SN 2023ixf (D. Perley & A. Gal-Yam 2023 and DESI). The SN 2024ggi +0.7 day spectrum was taken from the LJT, and the +9.6 day and +17.7 day spectra were both taken from the Lulin 1 m telescope.

2.4. PS1

In order to supplement our high-cadence SLT photometry, we obtained additional photometric follow-up with the 1.8 m PS1 telescope in Hawaii (K. C. Chambers et al. 2016) in the $grizy_{\rm PS}$ filter system (J. L. Tonry et al. 2012). PS1 is equipped with a 1.4 gigapixel camera with a $0\farcs26$ pixel scale and a 7 $\deg^2$ field of view. The images were processed using the Image Processing Pipeline (E. A. Magnier et al. 2020a). PS1 3π survey data were used as reference for image subtraction, and PS1 reference stars in the field were used for zero-point calibration (E. A. Magnier et al. 2020b).

2.5. Neil Gehrels Swift

SN 2024ggi was also observed with the Ultra-Violet/Optical Telescope (UVOT; P. W. A. Roming et al. 2005) on board the Neil Gehrels Swift observatory[34] (N. Gehrels et al. 2004). The UVOT photometry was performed using the task `uvotsource` within HEASoft version 6.25, with a 5″ aperture. We do not perform host subtraction. We note that the SN is saturated in the *u*-band images from MJD 60413 to 60422. We do not report the saturated magnitudes or use them for any further analysis in this paper.

2.6. Spectroscopic Classification and Follow-up

2.6.1. Li-Jiang 2.4 m Telescope

The classification spectrum of SN 2024ggi (Q. Zhai et al. 2024b) was obtained at Li-Jiang Observatory of Yunnan Observatories using the Li-Jiang 2.4 m telescope (hereafter LJT; Y.-F. Fan et al. 2015) equipped with the Yunnan Faint Object Spectrograph and Camera (YFOSC; C.-J. Wang et al. 2019) on MJD 60411.608. This spectrum underwent standard reduction procedures in IRAF, encompassing wavelength and flux calibration as well as correction for telluric absorptions. The spectral resolution of these data is estimated to be

[34] PIs: Sand, Schulze, Hoogendam, Zimmerman, Ravi.

Table 1
Photometry and Spectroscopy Observational Log of SN 2024ggi

Imaging					
$T_{start} - T_0$ (days)	MJD	Telescope	Instrument	Filter	Apparent Magnitude (AB mag)
−5.84	60405.063	ATLAS	ACAM	*o*	>19.80
+0.24	60411.141	ATLAS	ACAM	*o*	18.90 ± 0.10
+0.58	60411.476	Lulin/SLT	Andor SDK2	*u*	17.12 ± 0.16
+0.58	60411.479	Lulin/SLT	Andor SDK2	*g*	16.40 ± 0.04
+0.59	60411.485	Lulin/SLT	Andor SDK2	*r*	16.39 ± 0.07
+0.59	60411.489	Lulin/SLT	Andor SDK2	*i*	16.22 ± 0.19
+0.59	60411.493	Lulin/SLT	Andor SDK2	*z*	16.53 ± 0.10
+0.69	60411.589	Swift	UVOT	*uvw*1	16.72 ± 0.05
+0.69	60411.591	Swift	UVOT	*u*	16.25 ± 0.05
+0.69	60411.592	Swift	UVOT	*b*	16.02 ± 0.05
+0.69	60411.592	Swift	UVOT	*uvw*2	16.94 ± 0.05
+0.70	60411.596	Swift	UVOT	*v*	15.95 ± 0.07
+0.70	60411.597	Swift	UVOT	*uvm*2	16.90 ± 0.05
+0.70	60411.605	Paramount	ZWO ASI6200MM Pro	Lum	15.43 ± 0.26*
+0.71	60411.610	TAM/RC 12	ASI174	BesselI	16.08 ± 0.12*
+1.48	60412.384	iTelescope 33	Apogee USB/Net	Red	13.32 ± 0.02*
+1.49	60412.388	iTelescope 33	Apogee USB/Net	Green	13.41 ± 0.01*
+1.49	60412.391	iTelescope 33	Apogee USB/Net	Blue	13.16 ± 0.01*
+1.68	60412.580	TAM/RC 12	ASI174	Lum	12.90 ± 0.01*
+2.69	60413.588	CCESO/Planewave CDK17	QHY163M	Green	12.21 ± 0.01*
+2.69	60413.588	CCESO/Planewave CDK17	QHY163M	Red	12.12 ± 0.01*
+2.69	60413.588	CCESO/Planewave CDK17	QHY163M	Blue	11.92 ± 0.01*
+5.43	60416.325	PS1	Gigapixel camera	*i*	12.07 ± 0.00
+5.43	60416.325	PS1	Gigapixel camera	*r*	12.02 ± 0.01
+5.43	60416.326	PS1	Gigapixel camera	*y*	12.24 ± 0.01
+5.43	60416.326	PS1	Gigapixel camera	*z*	12.20 ± 0.01
+5.43	60416.327	PS1	Gigapixel camera	*w*	12.07 ± 0.00
+9.67	60420.573	TAM/RC 12	ASI174	Green	11.99 ± 0.03*
+9.68	60420.575	TAM/RC 12	ASI174	Blue	11.97 ± 0.03*

Note. Magnitudes have not corrected for the expected foreground and host extinction. The errors for the optical photometry are quoted to 1σ, while upper limits are quoted to 3σ significance. T_0 is at MJD = 60410.90 (explosion epoch). The magnitudes of citizen science images marked with an asterisk using non-*griz* filters are converted to *g*, *r*, and *i* using the formulae provided in Appendix C.

(This table is available in its entirety in machine-readable form in the online article.)

approximately 460, determined from the full width at half-maximum (FWHM) of the skylines. The spectrum obtained by LJT matches a young SN II with flash features due to SN–CSM interaction (see Figure 1). The redshift estimate from the average of the narrow Hα and Hβ lines is $z = 0.00214$.

2.6.2. Lulin One-meter Telescope

Follow-up optical spectra were obtained using the Lulin One-meter Telescope (LOT) with LISA, a commercial spectrograph produced by the Shelyak company, with a resolving power of around 1000 using a 300 line mm^{-1} grating and 35 μm slit. Adopting the primary QSI 660w CCD camera, it provides wavelength coverage between 3700 and 8400 Å with a pixel resolution of 1.82 Å. We followed the standard analytic process to subtract the bias and dark and flatten the 2D spectral image with the dome flat illuminated by a tungsten lamp. To perform the wavelength calibration, the built-in ArNe lamps were used. We selected spectrophotometric standards observed at a similar elevation to the target to construct the response curve along the wavelength channel to rebuild the relative intensity of our observation. We used the standard stars HR 7596 on 2024 April 20 and HIP 47431 on 2024 April 28. However, we caution that since the observations were of a target of opportunity on a moist night, especially at a high air mass of ∼2.9, they may result in an imperfect sensitivity correction in the blue end. The spectroscopic observations are detailed in Table 2, and the extinction-corrected spectra are presented in Figure 1. All observed spectra were uploaded to WISeREP (O. Yaron & A. Gal-Yam 2012). We highlight this is the first coordinated observation for SN follow-up from the Lulin Observatory, combining spectroscopic observations using LOT with simultaneous photometric observations using SLT.

3. Analysis

3.1. Precursor Search for SN 2024ggi

We employed the ATLAS Clean (ATClean; S. Rest et al. 2025) package to search for possible precursors in difference images from the ATLAS survey. ATClean forces photometry at the position of transients in historical ATLAS data (in the difference images) and analyzes the results by cleaning the individual measurements using statistical methods and the flux, uncertainty, and PSF measurements on the detector. Systematic residuals in the images that arise from detector artifacts, nearby sources, or imperfect image subtraction can all mimic an

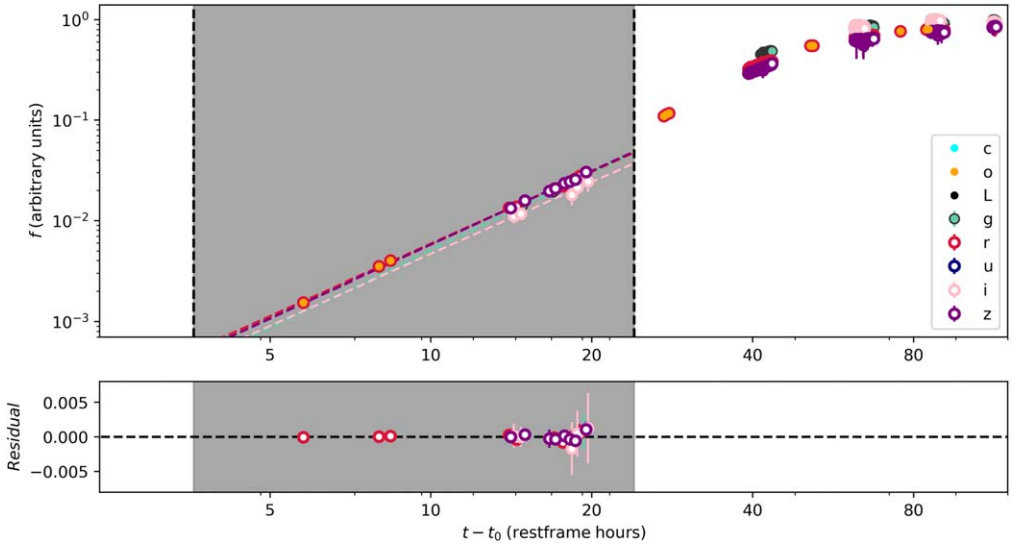

Figure 2. This figure presents the best-fit broken power-law fit to the early optical light curves in order to check the existence of shock cooling breakouts. The vertical gray shaded area indicates the time interval adopted for the light-curve fitting. The residuals are shown in the lower panel. The error bars shown represent 1σ uncertainties of magnitudes.

Table 2
Spectroscopy Observational Log of SN 2024ggi

Spectroscopy					
$T_{\rm start} - T_0$ (days)	MJD	Telescope	Instrument	Exp. Time (s)	Wavelength Range (Å)
+0.70	60411.608	LJT	YFOSC	1800	3611–8929
+9.64	60420.539	LOT	LISA	1800	3700–8436
+17.73	60428.633	LOT	LISA	300 × 3	3700–8436

Note. T_0 is at MJD = 60410.90 (explosion epoch).

astrophysical flux excess. ATClean uses control light curves around a source, which involves forcing multiple photometric measurements close to the source and comparing the statistical significance of the photometry forced at the source with that in the control fields. These control light curves are utilized to clean the photometry and calculate more robust detection limits for potential pre-SN eruptions than just forcing at the position of SN 2024ggi alone. With this method, we do not find any evidence for any significant real, astrophysical, excess flux in the historical ATLAS 6.5 yr data between MJD = 58065 (2017 November 8) and 60405 (2024 April 5).

S. Rest et al. (2025) describe how we can estimate the efficiency of recovery of a simulated precursor with a certain flux and duration using a Gaussian profile for the flux of a precursor event. The longer the duration of the precursor, the larger the time window we can bin over, allowing us to probe fainter fluxes for longer-duration simulated precursors. We have 90% detection efficiency for simulated Gaussian eruptions with $\sigma_{\rm sim} \geqslant 80$ days with peaks $o = 20.5$ mag. For shorter-duration events, we have shallower detection limits of 90% efficiency at 17.5, 19.5, and 20 mag for $\sigma_{\rm sim} = 5$, 20, and 40 days, respectively. We concluded that there is no evidence of a precursor. Our result is consistent with M. Shrestha et al. (2024), who do not detect any precursor emission for SN 2024ggi down to −9 mag.

3.2. SBO Signal Search

Constraining the explosion epoch is crucial to calculating accurate rise times and other light-curve fitting endeavors. As discussed in Appendix B, we modeled the early rise of light curves for SN 2024ggi using power-law fits similar to those in A. A. Miller et al. (2020) and determined the explosion epoch to be MJD $60410.90^{+0.08}_{-0.12}$, which will be used throughout the paper.

The power-law fits were also used to search for potential SBO emissions in the early light curves of SN 2024ggi, similar to what was found in the early data of SN 2023ixf. As shown in the lower panel of Figure 2, we present our multiband light curves collected within 4 days after the explosion. A power-law fit was applied to the early phases (i.e., the first ∼1 day, following the procedure used in G. Li et al. 2024 for SN 2023ixf), and no clear variances between the data and fits were observed, indicating that no apparent SBO features appeared. M. Shrestha et al. (2024) modeled the SN 2024ggi light curve over an extended period using two power-law components but did not identify any significant excess. As our data are taken earlier, we focused exclusively on the first day's data and applied a single power-law fit to emphasize the early evolution. One might argue that the absence of SBO in our data is due to observational limits; however, it could also indicate the presence of a dense, extended CSM around the RSG. This

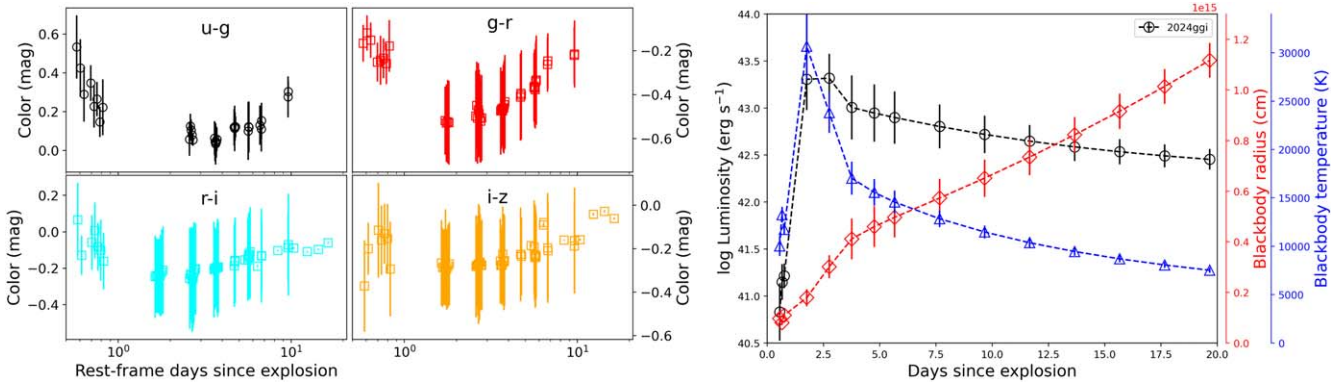

Figure 3. Left panel: the early-phase optical color evolution of SN 2024ggi, including $u-g$, $g-r$, $r-i$, and $i-z$. Right panel: blackbody inferred bolometric light curve (black), temperature (blue), and radius (red) evolution of SN 2024ggi.

scenario is further supported by other analyses, such as early colors, as discussed throughout the paper.

3.3. Photometric Behaviors and Color Evolution

We describe the photometric behaviors and color evolution of SN 2024ggi in this section, while the comparisons toward other SNe are detailed in Section 4.2. To estimate the photometric behaviors and align observations from different bands for spectral energy distribution (SED) construction, such as calculating colors, performing blackbody fits, etc., we interpolate our multiband light curves using HAFFET (S. Yang & J. Sollerman 2023). Given that 2024ggi clearly exhibits characteristics of a Type IIP SN, we opt to utilize the analytical function outlined in V. A. Villar et al. (2019). With the interpolated light curves, we found that the plateau occurred at $r = 12.02 \pm 0.09$ mag (after extinction correction) after 3.6 rest-frame days postexplosion. In other bands, the photometric behavior followed a similar trend until ∼18 days postexplosion, except for *uvm*2 and *uvw*2, which exhibited slight declines instead of plateauing. It is evident that SN 2024ggi experienced a rapid rise in the first few days, with a rise of 6.78 mag (r band) in 3.6 days or less, indicating a slope greater than 1.88 mag day^{-1}. Following this initial rise, a plateau phase of 18+ days (up to the current time) ensued, firmly establishing SN 2024ggi as a Type IIP SN. However, the plateau is not entirely flat. According to our analytic model fitting, there is an obvious decline that levels off in the UV bands, i.e., the Swift *u*, *uvm*2, and *uvw*2 bands, while in the red filters, i.e., the r and i bands, the light-curve plateau is relatively flat. We are only able to see these subtleties thanks to our well-sampled light curve of SN 2024ggi.

In the left panel of Figure 3, we investigate the optical color evolution of SN 2024ggi. All the colors were obtained by aligning the photometry in different bands using a 1 day bin. As shown, while other bands generally remain constant, the $u-g$ color decreases rapidly from 0.5 to 0 mag within just 6 hr, observed ∼0.57 day after the explosion. Without the dense confined CSM, the color is expected to simply become redder with time. The observed initial blue evolution followed by the red evolution can be explained by the existence of dense confined CSM (e.g., T. J. Moriya et al. 2018). Moreover, J. Zhang et al. (2024b) found that the SBO of SN 2024ggi might happen about 32 hr after the SN explosion due to the fluctuation of ionization states when the [C IV] λλ5801, 5811 were apparent in the spectrum. All of these findings support the scenario of a dense, confined CSM surrounding the RSG progenitor.

3.4. Bolometric Light Curve, Temperature, and Radius Evolution

We construct a bolometric light curve using the multiband photometry obtained for SN 2024ggi. To ensure that the fluxes are based more on observational data rather than solely on predictions, we matched photometric epochs using a 1 day bin and selected those epochs with observations in more than three bands. The remaining wavelength fluxes were estimated using analytic models outlined in V. A. Villar et al. (2019), as described in Section 3.3. Subsequently, we fit a blackbody spectrum to each of these single-epoch SEDs using methods similar to Superbol (M. Nicholl 2018) to derive the bolometric luminosity, temperature, and photospheric radius, shown in the right panel of Figure 3. As illustrated, we find the temperature at 0.6 day to be 10,000 K, peaking at 31,000 K at +1.7 days postexplosion epoch. These temperatures are consistent with those found by W. V. Jacobson-Galán et al. (2024) and M. Shrestha et al. (2024) and slightly higher at the peak than those reported by X. Chen et al. (2024), who did not include UV data for temperature calculations. The peak temperature for SN 2024ggi is close to that observed for SN 2023ixf by E. A. Zimmerman et al. (2024). The implied radius at our first epoch, at 0.6 day postexplosion, is $\sim 0.8 \times 10^{14}$ cm ($\sim 1149\ R_\odot$), which is smaller than the radius calculated for SN 2023ixf of $\sim 1.9 \times 10^{14}$ cm ($\sim 2731\ R_\odot$) by E. A. Zimmerman et al. (2024). From the progenitor observations, D. Xiang et al. (2024) estimated an initial progenitor radius of approximately $900\ R_\odot$; this suggests that the photosphere has expanded outward at a velocity of only 3500 km s^{-1}, which is relatively slow for less than 1 day after explosion. This may indicate a significant amount of mass overlaying the progenitor or that the photosphere is also receding inward in Lagrangian coordinates as the photospheric temperature rapidly cools.

3.5. Spectroscopic Properties

Our +0.7 day classification spectrum of SN 2024ggi shows narrow emissions of high-ionization species, known as flash features, as in Figure 1. Comparing with the +1.36 day spectrum of SN 2023ixf and lines identified from K. A. Bostroem et al. (2023) and J. Zhang et al. (2023), we detected the Balmer series (Hα, Hβ, Hγ, Hδ), He I λ6678.15, λ7065.19, C III (possible λ4056.0), λλ4647.5, 4650.0, λ5695.9, N III

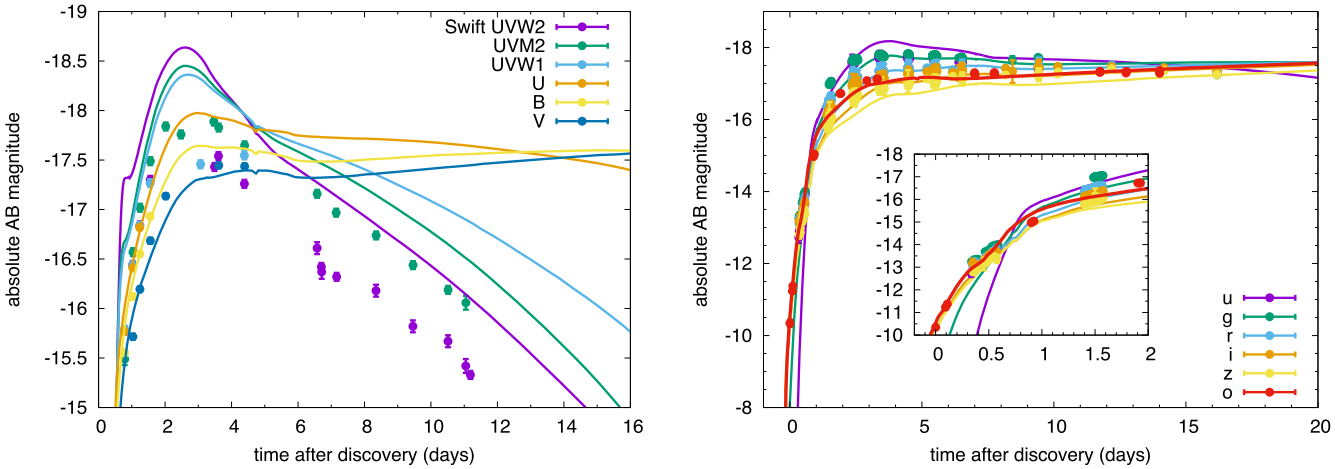

Figure 4. Left panel: light-curve modeling for SN 2024ggi in the Swift observed wavelength. Right panel: light-curve modeling for SN 2024ggi in the optical bands.

λ4097.33, $\lambda\lambda$4634.0, 4640.64, λ4858.82 (blended with Hβ), and possible N IV lines blended with the He I line. We did not detect the O III lines seen in SN 2023ixf.

We measured the P Cygni absorption of the H_β line at +9.6 days and +17.7 days, with velocities of 8400 $\pm$ 400 km s^{-1} at +9.6 days, decreasing slightly to 8300 $\pm$ 300 km s^{-1} at +17.7 days. This decline is consistent with the H_β velocity reported by M. Shrestha et al. (2024) at +5.5 days, which was approximately 9000 km s^{-1}. The Fe II λ5169 line is only visible in the +17.7 day spectrum, with a measured velocity of approximately 7300 km s^{-1}. The spectroscopic velocity measurement is significantly higher than the photospheric velocity derived from a blackbody fit to the SED of SN 2024ggi, which was $\sim$3500 km s^{-1} at +0.6 day. This indicates that the SN is undergoing substantial cooling over the course of a few hours, causing the photosphere to move inward in Lagrangian coordinates (i.e., relative to the ejecta).

We compare the spectroscopic evolution of SN 2024ggi with the nearby SN IIP 2023ixf that also exhibits flash features.[35] SN 2024ggi shows significant similarity to SN 2023ixf. Flash features are present in the first-day spectrum but disappear by +9.6 days, leaving a blue, featureless spectrum with emerging Hβ. By +17.7 days, the P Cygni profiles of Hβ, Hγ, and Hδ are visible, though the Hα absorption component is not yet present. SN 2023ixf also lacks this absorption at a similar epoch. In the +17.7 day spectrum of SN 2024ggi, all Balmer P Cygni profiles have blueshifted emission peaks. We measured a velocity of $-$2100 km s^{-1} from the Hα emission. J. P. Anderson et al. (2014) systematically studied this phenomenon and concluded that blueshifted emission-peak offsets are a generic property of photospheric-phase Type II SNe, with a mean value of $-$2000 km s^{-1} around +30 days.

4. Discussions

4.1. Modeling Results

To constrain the confined CSM properties based on the early-phase light curves, we searched for the best-matching models from the precomputed light-curve library presented in T. J. Moriya et al. (2023). The light-curve library contains multifrequency light curves from the explosions of the solar-metallicity RSG SN progenitors with a zero-age main-sequence ZAMS mass of 10–18 $M_\odot$ computed by T. Sukhbold et al. (2016). The light curves are computed by the 1D radiation hydrodynamics code STELLA (S. I. Blinnikov et al. 1998, 2006; S. Blinnikov et al. 2000). The model library covers explosion energies of 0.5–5 $\times$ 10^{51} erg and ^{56}Ni masses of 0.001–0.3 $M_\odot$. All the models are assumed to have a confined CSM. The mass-loss rates and radii of the confined CSM are assumed to be in the ranges of 10^{-5}–10^{-1} $M_\odot$ yr^{-1} and 10^{14}–10^{15} cm, respectively. The terminal wind velocity is assumed to be 10 km s^{-1} with the wind acceleration parameters β in the range of 0.5–5. We refer to T. J. Moriya et al. (2023) for further details of the model library.

We consider solar metallicity for SN 2024ggi in our model assumption based on host galaxy studies. Investigations by N. Kacharov et al. (2018) indicate NGC 3621 to already be very metal-rich in its early time. While studying the circumstellar environment around the progenitor, W. V. Jacobson-Galán et al. (2024) have indicated the presence of solar-metallicity CSM. The analysis by D. Xiang et al. (2024) indicates that the progenitor star is the reddest and most distinct among the red stars in the nearby vicinity, which too leads them to assuming solar metallicity. Further, X. Chen et al. (2024) also fit the solar-metallicity isochrones to estimate the constraints over the range of progenitor mass.

Because we focus on the early phase in the light curves that are mainly affected by the dense confined CSM, we do not constrain the ^{56}Ni mass in this paper. Similarly, because the early interaction signature is dominated by the CSM interaction, the progenitor mass is not well constrained, although we did not fix the progenitor mass in searching for matching light-curve models. We searched for a model that matches the optical luminosity evolution in all bands well by eye. The best-matching model we found is presented in Figure 4. The model has a explosion energy of 2 $\times$ 10^{51} erg, a mass-loss rate of 10^{-3} $M_\odot$ yr^{-1} (with the assumed 10 km s^{-1} wind), a confined CSM radius of 6 $\times$ 10^{14} cm, and β = 4.0. The corresponding CSM mass is 0.4 $M_\odot$. The previous mass-loss rate estimate by W. V. Jacobson-Galán et al. (2024) is slightly higher (10^{-2} $M_\odot$ yr^{-1} with 50 km^{-1}), but their estimated explosion energy (1.2 $\times$ 10^{51} erg) and confined CSM radius (4 $\times$ 10^{14} cm) are slightly lower. This model has a progenitor

[35] The comparison spectra were downloaded from WISeREP for SN 2023ixf (D. Perley & A. Gal-Yam 2023 and DESI). All spectra were calibrated for Milky Way and host extinction, with phases relative to the explosion time. We used $E(B-V)$ total = 0.04 mag and MJD 60082.788 for SN 2023ixf (G. Li et al. 2024)

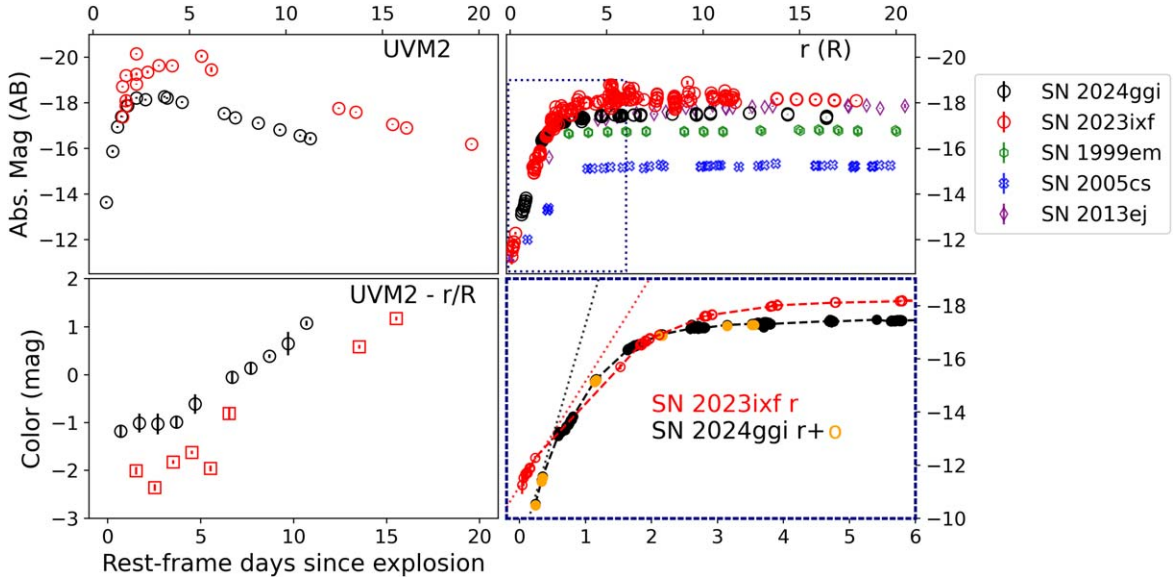

Figure 5. *uvm*2- and *r*-/*R*-band light curves, as well as their colors, compared to SN 2024ggi, SN 2023ixf, and other Type IIP SNe. Upper left panel: *uvm*2-band light curves. Upper right panel: *r*/*R*-band light curves. Bottom left panel: *uvm*2 − *r*/*R* colors. Bottom right panel: a zoom-in view of the *r*-band light curves, with the adopted Villar analytic model depicted by dashed lines and linear fits of the early rise indicated by dotted lines.

ZAMS mass of $12\,M_{\odot}$, but the ZAMS mass is difficult to constrain in this phase.

Our model has a higher UV luminosity than observed. If we try to match the UV luminosity, the optical luminosity becomes lower than observed, and we did not find a good model matching both optical and UV. Similarly, the light-curve model presented in W. V. Jacobson-Galán et al. (2024) matches well in UV, but their optical luminosity is fainter than observed. These discrepancies may originate from uncertainties in extinction estimates as well as the assumption of spherical symmetry in both models.

Using the same model grid, T. J. Moriya & A. Singh (2024) and A. Singh et al. (2024) estimated the properties of SN 2023ixf. The mass-loss rate is estimated to be around $10^{-2}\,M_{\odot}\,\mathrm{yr}^{-1}$ with $10\,\mathrm{km}^{-1}$ with the confined CSM radius of around 6×10^{14} cm with the explosion energy of 2×10^{51} erg. The CSM mass is $0.85\,M_{\odot}$. The estimated mass-loss rate and thus CSM mass for SN 2024ggi are slightly lower than those of SN 2023ixf.

4.2. Comparison with Other SNe II

We selected well-observed and well-understood typical Type II SNe as a comparison sample, covering a wide range of luminosities (SNe 2013ej, 1999em, 2005cs, in order from bright to faint). This sample also includes SNe with spectra that exhibit flash features (SN 2023ixf). The upper panels in Figure 5 present the *uvm*2- and *r*-/*R*-band light curves along with their colors in the bottom left panel. SN 2024ggi is slightly fainter in the *r* band compared to SN 2023ixf, with −17.8 mag at the plateau. The UV light curve of SN 2024ggi shares the same decay trend as that of SN 2023ixf but appears fainter. Meanwhile, its optical light curve is relatively flat, also resembling that of SN 2023ixf, though slightly dimmer. Therefore, compared to SN 2023ixf, SN 2024ggi is redder; however, it remains relatively blue when compared to other Type II SNe. Another noteworthy phenomenon is that SN 2024ggi exhibited a much faster rise (black dotted line) compared to SN 2023ixf (red dotted line) in the bottom right panel. This indicates that the CSM of SN 2024ggi is less dense than that of SN 2023ixf, although the CSM density is still high enough to affect their light curves and spectra in the early phases.

5. Conclusion and Future Prospects

The ATLAS early (6 hr after the SN explosion) detection and subsequent high-cadence monitoring with the Kinder project of SN 2024ggi (between 14 and 20 hr after the explosion) have provided a wealth of data that are invaluable for understanding the early stages of SN evolution. All these photometric (e.g., getting bluer rapidly) and spectroscopic behaviors indicate a wind SBO scenario.

The blackbody fitting indicates a radius of $\sim0.8\times10^{14}$ cm at 0.6 day postexplosion, suggesting a photospheric expansion velocity of $3500\,\mathrm{km\,s}^{-1}$. This slow expansion may imply a significant amount of overlying mass on the progenitor or an inward recession of the photosphere in Lagrangian coordinates as the temperature rapidly cools.

The radiation time of the SBO is related to the progenitor's size, and a dense CSM can make the SBO brighter and longer-lasting. Therefore, comprehensive coverage is crucial for capturing the SBO and studying the diversity of the SN progenitors. Our observational data contain gaps that may lead to missing the SBO signal. To address this limitation, we emphasize the importance of future efforts involving additional observational facilities and the active participation of amateur astronomers. Such collaborations would help bridge these gaps and enhance the detection of early SBO features. Statistics from the Zwicky Transient Facility bright transient survey (C. Fremling et al. 2020; D. A. Perley et al. 2020) indicate that, on average, one SN peaks brighter than 15 mag every 2 months. These bright SNe are ideal targets for citizen astronomers. High-cadence continuous follow-up is essential to capture the SBO signal. Achieving this is impossible at a single site, but it is an ideal project for a global observational network coordinating with citizen scientists. Such a strategy was applied in the case of SN 2023ixf

(G. Hosseinzadeh et al. 2023; G. Li et al. 2024). Now, with SN 2024ggi, we provide another example that demonstrates that citizen scientists responded rapidly to follow-up and the benefits of collaborative high-cadence observations.

Acknowledgments

We thank Chi-Sheng Lin and Jhen-Kuei Guo for Kinder observations and IT support and citizen astronomers Wen-Li Kuo and Pei-Lun Wang for providing the SN JPG images. T.-W.C. thanks Yi-Zhen Lin for administrative assistance to the GREAT Lab. K.K.M. thanks Tommy Tse and David Cheng for the dedicated efforts in observing the supernova despite the less-than-ideal weather conditions. T.-W.C. and A.A. acknowledge the Yushan Young Fellow Program by the Ministry of Education, Taiwan, for the financial support (MOE-111-YSFMS-0008-001-P1). S.Y. and Z.-N.W. are supported by the National Natural Science Foundation of China under grant No. 12303046 and the Henan Province High-Level Talent International Training Program. Numerical computations were in part carried out on the PC cluster at the Center for Computational Astrophysics, National Astronomical Observatory of Japan. This work was supported by the JSPS Core-to-Core Program (grant No. JPJSCCA20210003). This work was funded by ANID, Millennium Science Initiative, ICN12_009. M.F. is supported by a Royal Society—Science Foundation Ireland University Research Fellowship. M.N. is supported by the European Research Council (ERC) under the European Union's Horizon 2020 research and innovation program (grant agreement No. 948381) and by UK Space Agency grant No. ST/Y000692/1. G.P. acknowledges support from ANID through Millennium Science Initiative Programs ICN12 009. H.F.S. is supported by the Eric and Wendy Schmidt AI in Science Fellowship. X.W. is supported by the National Natural Science Foundation of China (NSFC grants 12288102 and 1203300) and the Tencent Xplorer Prize. J.Z. is supported by the National Key R&D Program of China with No. 2021YFA1600404, the National Natural Science Foundation of China (12173082), the Yunnan Province Foundation (202201AT070069), the Top-notch Young Talents Program of Yunnan Province, the Light of West China Program provided by the Chinese Academy of Sciences, the International Centre of Supernovae, Yunnan Key Laboratory (No. 202302AN360001). We acknowledge WISeREP (https://www.wiserep.org). This work has made use of data from the Asteroid Terrestrial-impact Last Alert System (ATLAS) project. The Asteroid Terrestrial-impact Last Alert System (ATLAS) project is primarily funded to search for near-Earth asteroids through NASA grants NN12AR55G, 80NSSC18K0284, and 80NSSC18K1575; by-products of the NEO search include images and catalogs from the survey area. This work was partially funded by Kepler/K2 grant J1944/80NSSC19K0112 and HST GO-15889 and STFC grants ST/T000198/1 and ST/S006109/1. The ATLAS science products have been made possible through the contributions of the University of Hawaii Institute for Astronomy, the Queen's University Belfast, the Space Telescope Science Institute, the South African Astronomical Observatory, and the Millennium Institute of Astrophysics (MAS), Chile. The Pan-STARRS1 Surveys (PS1) and the PS1 public science archive have been made possible through contributions by the Institute for Astronomy, the University of Hawaii, the Pan-STARRS Project Office, the Max Planck Society and its participating institutes, the Max Planck Institute for Astronomy, Heidelberg, and the Max Planck Institute for Extraterrestrial Physics, Garching, The Johns Hopkins University, Durham University, the University of Edinburgh, the Queen's University Belfast, the Harvard-Smithsonian Center for Astrophysics, the Las Cumbres Observatory Global Telescope Network Incorporated, the National Central University of Taiwan, the Space Telescope Science Institute, the National Aeronautics and Space Administration under grant No. NNX08AR22G issued through the Planetary Science Division of the NASA Science Mission Directorate, the National Science Foundation grant No. AST-1238877, the University of Maryland, Eotvos Lorand University (ELTE), the Los Alamos National Laboratory, and the Gordon and Betty Moore Foundation. This research is based on observations made with the mission, obtained from the MAST data archive at the Space Telescope Science Institute, which is operated by the Association of Universities for Research in Astronomy, Inc., under NASA contract NAS 5-26555. This publication has made use of data collected at Lulin Observatory, partly supported by MoST grant 109-2112-M-008-001.

Facilities: ATLAS, Swift, PS1, LO:1m.

Software: ChatGPT,[36] IRAF (D. Tody 1986; D. Tody 1993), astropy (Astropy Collaboration et al. 2013; Astropy Collaboration et al. 2018), HAFFET (S. Yang & J. Sollerman 2023), scipy (P. Virtanen et al. 2020), numpy (C. R. Harris et al. 2020), SExtractor (E. Bertin & S. Arnouts 1996), hotpants (A. Becker 2015), matplotlib (J. D. Hunter 2007), emcee (D. Foreman-Mackey et al. 2013).

Appendix A
Observational Log

We give our observational log for photometric and spectroscopic follow-up in Tables 1 and 2. We only list the first epoch of each band; the full table in machine-readable format is available. We characterize the early emission of SN 2024ggi as shown in Figure 6.

Appendix B
Power-law Fits for the Explosion Epoch

W. V. Jacobson-Galán et al. (2024) fit the bolometric light curve of SN 2024ggi to a suite of hydrodynamical models, constraining the time of first light to MJD = $60410.56^{+0.07}_{-0.12}$. In this paper, we use the Bayesian framework developed by A. A. Miller et al. (2020) to model the early rise of light curves simultaneously in multiple bands as a power law. This approach assumes that the epoch of first light is the same across different bands, which is reasonable given the observation cadence and the similarity of SN ejecta opacity at these wavelengths, and we apply this framework to the *g* and *r* bands simultaneously. To establish the flux light-curve baselines and increase observation cadence, we included ATLAS pre- and postdiscovery observations, assuming similar filter transmission between the SDSS *r* (*g*) and ATLAS *o* (*c*) bands. We note that a nondetection was reported by the GOTO team in their *L* band, which can effectively constrain the flux baselines as well. Given that the *L* band has a broad transmission covering both *g* and *r*, we could include it as a baseline point for both bands. We employed a Markov Chain Monte Carlo approach via emcee[37] to derive the fitted power-law models, testing various methods, i.e., fitting from the flux baseline up to 40% or 60%

[36] ChatGPT serves as a grammar checker and paraphrasing tool; OpenAI. (2022). Introducing ChatGPT. https://openai.com/blog/chatgpt

[37] emcee.readthedocs.io

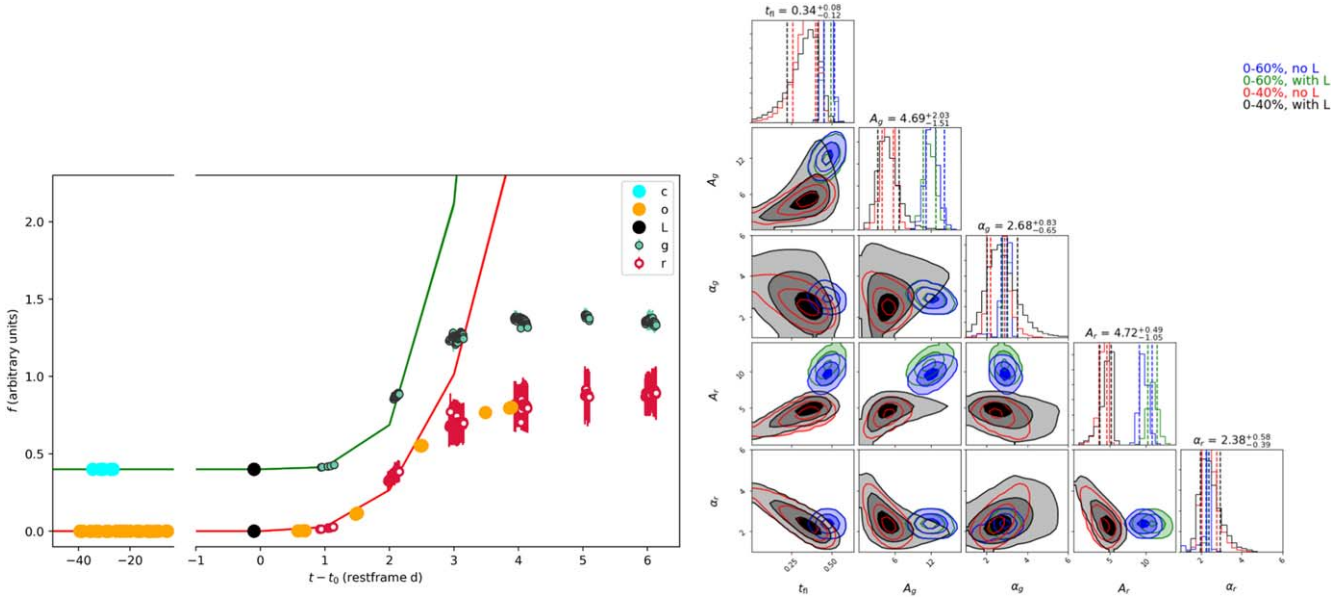

Figure 6. Left panel: power-law fits to the early g- (c-) and r- (o-) band light curves in order to estimate the explosion epoch as well as rising profiles, e.g., power-law indices. The solid lines represent the best-fit power-law models, fitted to photometric data (together with the GOTO L-band limits) ranging from the flux baseline up to 40% of the maximum. Right panel: contour plots for the power-law fitting parameters are presented, with different colors representing various fitting methods. These methods include fitting from the flux baseline up to 40% or 60% of the maximum, both with and without the GOTO L-band limits. For each method, the converged parameters are shown within three dashed regions corresponding to 1σ, 2σ, and 3σ levels.

of the maximum, both with and without the GOTO L-band limits. As in R. P. Olling et al. 2015 and A. A. Miller et al. 2020, we follow their approach and use 40% of the maximum flux for the early light curves. However, we also tested the 60% flux interval to include additional SLT data and to assess how this affects the fits. Using all the aforementioned assumptions and the HAFFET tool (S. Yang & J. Sollerman 2023), we characterize the early emission of SN 2024ggi as shown in Figure 6. Its left panel displays the early light curves of SN 2024ggi along with the best-fit power-law models, while the right panel shows the converged Monte Carlo samples as contours. For this analysis, we used the explosion epoch outlined in W. V. Jacobson-Galán et al. (2024) as our initial reference. Our subsequent power-law fits confirmed this explosion epoch, revealing only a 0.34 day offset. As a result, we constrained the explosion epoch to MJD $60410.90^{+0.08}_{-0.12}$, which will be used throughout the paper. Meanwhile, the power-law fits yielded indices of $2.68^{+0.83}_{-0.65}$ and $2.38^{+0.58}_{-0.39}$ for the g and r bands, respectively, indicating a faster rise for SN 2024ggi compared to typical SNe IIP.

Appendix C
Citizen Science Image Calibration

The citizen science images in this work were taken by four different sets of instruments. (1) TAM, a 30 cm reflector with CCD and L, G, B, and Bessel I filters at Lulin Observatory operated by TAM. (2) Paramount, a 13 cm refractor with a CMOS camera and L filter owned and operated by Tommy Tse and David Cheng at the HK Remote Observatory Team at Lijiang Gemini Observatory. The images are provided by Ka Kit Man. (3) iTelescope 33, a 32 cm f/9 reflector with CCD and G, R, and B filters at Siding Spring Observatory, Australia. The images are provided by Yu-Chien Shiau. (4) CCESO, a 43 cm reflector with CCD and G, R, and B filters at CCESO, Taiwan. While the LRGB filter sets of the four telescopes are not exactly the same, they are mostly consistent with $L \sim$ SDSS $g' + r'$, which has transparency from 400 to 700 nm, and the RGB filters roughly equally divide the wavelength coverage of SDSS $g' + r'$. All of the citizen science images were reduced under the standard CCD reduction procedure, which include the bias and dark current subtraction and flat calibration. After removing the instrumental trends, all of the images were calibrated and measured the photometry zero-points against the SkyMapper photometry system (C. Wolf et al. 2018) by cross-matching the on-field sources with Gaia star catalogs and SkyMapper source catalogs. We found the color conversion between our citizen science instruments and the SkyMapper photometry system by solving one of the following equations:

$$m_{\rm citi} - m_{\rm sm} = C_0 + C_1\,(g - r)_{\rm sm} \tag{C1}$$

or

$$m_{\rm citi} - m_{\rm sm} = C_0 + C_1\,(g - r)_{\rm sm} + C_2\,(g - r)^2_{\rm sm}. \tag{C2}$$

Here $m_{\rm citi}$ and $m_{\rm sm}$ are the citizen science images and SkyMapper magnitude, respectively; C_0 is a constant; C_1 is the coefficient of the linear color term; and C_2 is the coefficient of the quadratic term. For the TAM system, we found

$$\begin{aligned} L - r_{\rm sm} &= -0.20 + 0.63\,(g - r)_{\rm sm} \\ &\quad - 0.19\,(g - r)^2_{\rm sm},\ {\rm rms} = 0.05, \\ G - r_{\rm sm} &= -0.27 + 0.72\,(g - r)_{\rm sm},\ {\rm rms} = 0.11, \\ B - g_{\rm sm} &= -0.20 + 0.760\,(g - r)_{\rm sm},\ {\rm rms} = 0.07, \\ I - i_{\rm sm} &= 0.02 - 0.02\,(r - i)_{\rm sm},\ {\rm rms} = 0.08; \end{aligned}$$

the EQMOD system,

$$L - r_{\rm sm} = -0.13 + 0.38\,(g - r)_{\rm sm},\ {\rm rms} = 0.18;$$

the iTelescope 33 system,

$$R - r_{\rm sm} = 0.07 - 0.17\,(g - r)_{\rm sm},\ \ {\rm rms} = 0.04,$$
$$G - r_{\rm sm} = -0.29 + 0.79\,(g - r)_{\rm sm},\ \ {\rm rms} = 0.05,$$
$$B - g_{\rm sm} = -0.25 + 0.72\,(g - r)_{\rm sm},\ \ {\rm rms} = 0.05;$$

and finally, the CCESO system,

$$R - r_{\rm sm} = -0.12 + 0.30\,(g - r)_{\rm sm},\ \ {\rm rms} = 0.03,$$
$$G - r_{\rm sm} = -0.16 + 0.40\,(g - r)_{\rm sm},\ \ {\rm rms} = 0.02,$$
$$B - g_{\rm sm} = -0.17 - 0.53\,(g - r)_{\rm sm},\ \ {\rm rms} = 0.03.$$

Appendix D
Host Galaxy and Extinction

SN 2024ggi occurs in NGC 3621, a bulgeless late-type (Sd) spiral galaxy (A. J. Barth et al. 2009) situated in the Hydra constellation. The location of the explosion site of SN 2024ggi is 110″ away from the galactic center (D. Xiang et al. 2024). NGC 3621 is face-on with an extended disk (B. S. Koribalski et al. 2004) and has an inclination angle of 25° (N. Kacharov et al. 2018). NGC 3621 is known to host an active galactic nucleus (S. Satyapal et al. 2007; M. Gliozzi et al. 2009) that is powered by a supermassive black hole of mass $\lesssim 3 \times 10^6\,M_\odot$ (A. J. Barth et al. 2009). Additionally, NGC 3621 has a stellar mass of $8.1 \times 10^9\,M_\odot$ (I. Y. Georgiev et al. 2016), an absolute B-band magnitude of -20.07 ± 0.23, and a star formation rate of $830 \pm 640\,M_\odot\,{\rm Myr}^{-1}$ in its star-forming nucleus (N. Kacharov et al. 2018).

Various methods are available to measure the distances of NGC 3621, including Cepheids, the Tully–Fisher relation, and the tip of the red giant branch (TRGB). However, considering the potential contamination from non-RGB populations in the TRGB method and the intrinsic scatter associated with the Tully–Fisher relation, we ultimately adopted the distance derived from Cepheids. The distance to the host galaxy, NGC 3621, is $d = 6.64 \pm 0.3$ Mpc, with a distance modulus of $\mu = 29.11 \pm 0.06$ mag (W. L. Freedman et al. 2001).

We consider the Milky Way foreground extinction of $E(B - V)_{\rm MW} = 0.070$ mag (E. F. Schlafly & D. P. Finkbeiner 2011) in the direction of SN 2024ggi. The presence of Na I D2 and D1 lines in the high-resolution KAST spectrum indicates host galaxy extinction, and W. V. Jacobson-Galán et al. (2024) estimate the corresponding host galaxy extinction of $E(B - V)_{\rm host} = 0.084 \pm 0.018$ mag. Thus, we consider a total (Milky Way + host) extinction of $E(B - V)_{\rm total} = 0.154 \pm 0.018$ mag in our analysis. The blended Na I D line was also detected in our LOT spectra of SN 2024ggi.

ORCID iDs

Ting-Wan Chen (陳婷琬) https://orcid.org/0000-0002-1066-6098
Sheng Yang (杨圣) https://orcid.org/0000-0002-2898-6532
Shubham Srivastav https://orcid.org/0000-0003-4524-6883
Takashi J. Moriya https://orcid.org/0000-0003-1169-1954
Stephen J. Smartt https://orcid.org/0000-0002-8229-1731
Sofia Rest https://orcid.org/0000-0002-3825-0553
Armin Rest https://orcid.org/0000-0002-4410-5387
Hsing Wen Lin (林省文) https://orcid.org/0000-0001-7737-6784
Hao-Yu Miao (繆皓宇) https://orcid.org/0000-0003-2736-5977
Yu-Chi Cheng (鄭宇棋) https://orcid.org/0000-0001-9686-5874
Amar Aryan https://orcid.org/0000-0002-9928-0369
Morgan Fraser https://orcid.org/0000-0003-2191-1674
Li-Ching Huang (黃立晴) https://orcid.org/0000-0002-9679-5279
Yu-Hsuan Liu (劉宇軒) https://orcid.org/0009-0005-2378-2601
Ken W. Smith https://orcid.org/0000-0001-9535-3199
Heloise F. Stevance https://orcid.org/0000-0002-0504-4323
Joseph P. Anderson https://orcid.org/0000-0003-0227-3451
Charlotte R. Angus https://orcid.org/0000-0002-4269-7999
Thomas de Boer https://orcid.org/0000-0001-5486-2747
Kenneth Chambers https://orcid.org/0000-0001-6965-7789
Hao-Yuan Duan (段皓元) https://orcid.org/0000-0002-7022-4742
Nicolas Erasmus https://orcid.org/0000-0002-9986-3898
Michael Fulton https://orcid.org/0000-0003-1916-0664
Hua Gao https://orcid.org/0000-0003-1015-5367
Mark E. Huber https://orcid.org/0000-0003-1059-9603
Chien-Cheng Lin (林建爭) https://orcid.org/0000-0002-7272-5129
Eugene A. Magnier https://orcid.org/0000-0002-7965-2815
Ka Kit Man (文家傑) https://orcid.org/0000-0001-7735-928X
Thomas Moore https://orcid.org/0000-0001-8385-3727
Chow-Choong Ngeow (饒兆聰) https://orcid.org/0000-0001-8771-7554
Matt Nicholl https://orcid.org/0000-0002-2555-3192
Po-Sheng Ou (歐柏昇) https://orcid.org/0000-0003-1295-8235
Giuliano Pignata https://orcid.org/0000-0003-0006-0188
Julian Silvester Sommer https://orcid.org/0000-0002-1154-8317
John L. Tonry https://orcid.org/0000-0003-2858-9657
Xiao-Feng Wang (王晓锋) https://orcid.org/0000-0002-7334-2357
Richard Wainscoat https://orcid.org/0000-0002-1341-0952
David R. Young https://orcid.org/0000-0002-1229-2499
You-Ting Yeh (葉祐廷) https://orcid.org/0009-0004-8836-5828
Jujia Zhang (张居甲) https://orcid.org/0000-0002-8296-2590

References

Anderson, J. P., Dessart, L., Gutierrez, C. P., et al. 2014, MNRAS, 441, 671
Astropy Collaboration, Price-Whelan, A. M., Sipőcz, B. M., et al. 2018, AJ, 156, 123
Astropy Collaboration, Robitaille, T. P., Tollerud, E. J., et al. 2013, A&A, 558, A33
Barth, A. J., Strigari, L. E., Bentz, M. C., Greene, J. E., & Ho, L. C. 2009, ApJ, 690, 1031
Becker, A. 2015, HOTPANTS: High Order Transform of PSF ANd Template Subtraction, Astrophysics Source Code Library, ascl:1504.004
Bertin, E., & Arnouts, S. 1996, A&AS, 117, 393
Blinnikov, S., Lundqvist, P., Bartunov, O., Nomoto, K., & Iwamoto, K. 2000, ApJ, 532, 1132
Blinnikov, S. I., Eastman, R., Bartunov, O. S., Popolitov, V. A., & Woosley, S. E. 1998, ApJ, 496, 454
Blinnikov, S. I., Röpke, F. K., Sorokina, E. I., et al. 2006, A&A, 453, 229
Bostroem, K. A., Pearson, J., Shrestha, M., et al. 2023, ApJL, 956, L5
Bruch, R. J., Gal-Yam, A., Schulze, S., et al. 2021, ApJ, 912, 46
Bruch, R. J., Gal-Yam, A., Yaron, O., et al. 2023, ApJ, 952, 119
Chambers, K. C., Magnier, E. A., Metcalfe, N., et al. 2016, arXiv:1612.05560
Chandra, P., Maeda, K., Nayana, A. J., et al. 2024, ATel, 16612, 1

Chen, T., Yang, S., Lin, H.-W., et al. 2023, TNSAN, 175, 1
Chen, T. W., Sankar.K, A., Yang, S., et al. 2024, TNSAN, 102, 1
Chen, T. W., Yang, S., Pan, Y.-C., et al. 2021, TNSAN, 92, 1
Chen, X., Kumar, B., Er, X., et al. 2024, ApJ, 971, L2
Fan, Y.-F., Bai, J.-M., Zhang, J.-J., et al. 2015, RAA, 15, 918
Foreman-Mackey, D., Hogg, D. W., Lang, D., & Goodman, J. 2013, PASP, 125, 306
Förster, F., Moriya, T. J., Maureira, J. C., et al. 2018, NatAs, 2, 808
Fossey, S. J., Cooke, B., Pollack, G., Wilde, M., & Wright, T. 2014, CBET, 3792, 1
Freedman, W. L., Madore, B. F., Gibson, B. K., et al. 2001, ApJ, 553, 47
Fremling, C., Miller, A. A., Sharma, Y., et al. 2020, ApJ, 895, 32
Gal-Yam, A., Arcavi, I., Ofek, E. O., et al. 2014, Natur, 509, 471
Gehrels, N., Chincarini, G., Giommi, P., et al. 2004, ApJ, 611, 1005
Georgiev, I. Y., Böker, T., Leigh, N., Lützgendorf, N., & Neumayer, N. 2016, MNRAS, 457, 2122
Gillanders, J. H., Rhodes, L., Srivastav, S., et al. 2024, ApJ, 969, L14
Gliozzi, M., Satyapal, S., Eracleous, M., Titarchuk, L., & Cheung, C. C. 2009, ApJ, 700, 1759
Goldberg, J. A., Jiang, Y.-F., & Bildsten, L. 2022, ApJ, 933, 164
González-Gaitán, S., Tominaga, N., Molina, J., et al. 2015, MNRAS, 451, 2212
Harris, C. R., Millman, K. J., van der Walt, S. J., et al. 2020, Natur, 585, 357
Hoogendam, W., Auchettl, K., Tucker, M., et al. 2024, TNSAN, 103, 1
Hosseinzadeh, G., Farah, J., Shrestha, M., et al. 2023, ApJL, 953, L16
Hunter, J. D. 2007, CSE, 9, 90
Itagaki, K. 2023, TNSTR, 2023-1158, 1
Jacobson-Galán, W. V., Davis, K. W., Kilpatrick, C. D., et al. 2024, ApJ, 972, 177
Kacharov, N., Neumayer, N., Seth, A. C., et al. 2018, MNRAS, 480, 1973
Killestein, T., Ackley, K., Kotak, R., et al. 2024, TNSAN, 101, 1
Komura, Y., Matsunaga, K., Uchida, H., & Enoto, T. 2024, ATel, 16595, 1
Koribalski, B. S., Staveley-Smith, L., Kilborn, V. A., et al. 2004, AJ, 128, 16
Kumar, B., Chen, X., Lin, W., et al. 2024, TNSAN, 108, 1
Li, G., Hu, M., Li, W., et al. 2024, Natur, 627, 754
Magnier, E. A., Chambers, K. C., Flewelling, H. A., et al. 2020a, ApJS, 251, 3
Magnier, E. A., Schlafly, E. F., Finkbeiner, D. P., et al. 2020b, ApJS, 251, 6
Marti-Devesa, G. & Fermi-LAT Collaboration 2024, ATel, 16601, 1
Miller, A. A., Yao, Y., Bulla, M., et al. 2020, ApJ, 902, 47
Moore, T., Gillanders, J., Nicholl, M., et al. 2025, ApJ, 980, L44
Moriya, T., Tominaga, N., Blinnikov, S. I., Baklanov, P. V., & Sorokina, E. I. 2011, MNRAS, 415, 199
Moriya, T. J., Förster, F., Yoon, S.-C., Gräfener, G., & Blinnikov, S. I. 2018, MNRAS, 476, 2840
Moriya, T. J., & Singh, A. 2024, PASJ, 76, 1050
Moriya, T. J., Subrayan, B. M., Milisavljevic, D., & Blinnikov, S. I. 2023, PASJ, 75, 634
Morozova, V., Piro, A. L., & Valenti, S. 2017, ApJ, 838, 28
Morozova, V., Piro, A. L., & Valenti, S. 2018, ApJ, 858, 15
Nicholl, M. 2018, RNAAS, 2, 230
Niemela, V. S., Ruiz, M. T., & Phillips, M. M. 1985, ApJ, 289, 52
Olling, R. P., Mushotzky, R., Shaya, E. J., et al. 2015, Natur, 7552, 332
Pearson, J., Sand, D. J., Lundqvist, P., et al. 2024, ApJ, 960, 29
Pérez-Fournon, I., Poidevin, F., Aguado, D. S., et al. 2024, TNSAN, 107, 1
Perley, D., & Gal-Yam, A. 2023, TNSCR, 2023-1164, 1
Perley, D. A., Fremling, C., Sollerman, J., et al. 2020, ApJ, 904, 35
Pessi, T., Cartier, R., Hueichapan, E., et al. 2024, A&A, 688, L28
Rest, S., Rest, A., Kilpatrick, C. D., et al. 2025, ApJ, 979, 114
Romanov, F. D. 2024, TNSAN, 109, 1
Roming, P. W. A., Kennedy, T. E., Mason, K. O., et al. 2005, SSRv, 120, 95
Ryder, S., Maeda, K., Chandra, P., Alsaberi, R., & Kotak, R. 2024, ATel, 16616, 1
Satyapal, S., Vega, D., Heckman, T., O'Halloran, B., & Dudik, R. 2007, ApJL, 663, L9
Schlafly, E. F., & Finkbeiner, D. P. 2011, ApJ, 737, 103
Shingles, L., Smith, K. W., Young, D. R., et al. 2021, TNSAN, 7, 1
Shrestha, M., Bostroem, K. A., Sand, D. J., et al. 2024, ApJL, 972, L15
Singh, A., Teja, R. S., Moriya, T. J., et al. 2024, ApJ, 975, 132
Smith, K. W., Smartt, S. J., Young, D. R., et al. 2020, PASP, 132, 085002
Srivastav, S., Chen, T. W., Smartt, S. J., et al. 2024, TNSAN, 100, 1
Sukhbold, T., Ertl, T., Woosley, S. E., Brown, J. M., & Janka, H. T. 2016, ApJ, 821, 38
Tody, D. 1986, Proc. SPIE, 627, 733
Tody, D. 1993, in ASP Conf. Ser. 52, Astronomical Data Analysis Software and Systems II, ed. R. J. Hanisch, R. J. V. Brissenden, & J. Barnes (San Francisco, CA: ASP), 173
Tonry, J., Denneau, L., Weiland, H., et al. 2024, TNSTR, 2024-1020, 1
Tonry, J. L., Denneau, L., Flewelling, H., et al. 2018b, ApJ, 867, 105
Tonry, J. L., Denneau, L., Heinze, A. N., et al. 2018a, PASP, 130, 064505
Tonry, J. L., Stubbs, C. W., Lykke, K. R., et al. 2012, ApJ, 750, 99
Villar, V. A., Berger, E., Miller, G., et al. 2019, ApJ, 884, 83
Virtanen, P., Gommers, R., Oliphant, T. E., et al. 2020, NatMe, 17, 261
Wang, C.-J., Bai, J.-M., Fan, Y.-F., et al. 2019, RAA, 19, 149
Waxman, E., & Katz, B. 2017, in Handbook of Supernovae, ed. A. W. Alsabti & P. Murdin (Berlin: Springer), 967
Wolf, C., Onken, C. A., Luvaul, L. C., et al. 2018, PASA, 35, e010
Xiang, D., Mo, J., Wang, X., et al. 2024, ApJL, 969, L15
Yang, S., Chen, T. W., Stevance, H. F., et al. 2024, TNSAN, 105, 1
Yang, S., & Sollerman, J. 2023, ApJS, 269, 40
Yang, S., Sollerman, J., Chen, T. W., et al. 2021, A&A, 646, A22
Yaron, O., Bruch, R., Chen, P., et al. 2023, TNSAN, 133, 1
Yaron, O., & Gal-Yam, A. 2012, PASP, 124, 668
Zhai, Q., Li, L., Wang, Z., Zhang, J., & Wang, X. 2024a, TNSAN, 104, 1
Zhai, Q., Li, L., Zhang, J., & Wang, X. 2024b, TNSCR, 2024-1031, 1
Zhang, J., Dessart, L., Wang, X., et al. 2024b, ApJL, 970, L18
Zhang, J., Li, C. K., Cheng, H. Q., et al. 2024a, ATel, 16588, 1
Zhang, J., Lin, H., Wang, X., et al. 2023, SciBu, 68, 2548
Zimmerman, E. A., Irani, I., Chen, P., et al. 2024, Natur, 627, 759